EDITORIAL BOARD

Annual Subscription

Pakistan: Rs 250 Foreign Countries: US$ 40 Overseas Air Mail Charges: US$ 10

The Journal is published bi-annually
In April and October

Published by:
Riaz Ahmad, Government College University, Lahore, Pakistan.
Printed at:

CONTENTS

PK ISSN 0022- 2941; CODEN JNSMAC
Vol. 57, (2017) PP 01-09

ON THE CENTRALITY MEASURES OF ECCENTRICITIES IN CONNECTED GRAPHS

ANTONY PUTHUSSERY[1] AND JOSEPH VARGHESE KUREETHARA[2]

[1] Assistant Professor, Faculty of Engineering, Christ University, frantony@christuniversity.in
[2] Associate Professor, Department of Mathematics, Christ University, frjoseph@christuniversity.in
Christ University, Bengaluru 560029

ABSTRACT

A graph G is defined to be a μ-graph if the standard measures of central tendencies (mean, median and mode) of eccentricities coincide. The μ-graphs are characterized and studied in this paper. The measures of central tendencies of the eccentricities of graphs have implications in the study of Chemical Graphs, Internet Graphs, Acquaintanceship Graphs, BIG DATA Analysis and Social Network Graphs, to name a few.

Keywords: Eccentricity; Mean Eccentricity; Median Eccentricity; Mode Eccentricity; μ –graph.

1. INTRODUCTION

By a graph G = (V, E), we mean a finite, undirected graph with neither loops nor multiple edges. For graph-theoretic terminology we refer to Harary [4]. All graphs in this paper are assumed to be connected and non-trivial.

The eccentricity of a vertex is the maximum distance from it to any other vertex. The radius of the graph is the minimum eccentricity, and the *diameter* is the maximum eccentricity. Nestled in between is the average eccentricity which is introduced by Buckley and Harary [1] (as the eccentric mean). In association with different centrality measures, many authors have investigated how the different parameters of distance are related. Mukambi and Hove-Musekaw [6] studied the cutting number of a graph in relation with the centrality. Later in 1995, Hage and Harary [3] analyzed the relation between eccentricity and centrality. But the notion of mean eccentricity seems not to have been studied extensively. Dankelmann *et al.*[2] established the bounds on the mean eccentricity of a graph. Kauffman [5] made an extensive study on mode vertices and mode graphs, in relation with the eccentricity of the vertices of a graph. In this paper, the sequence of eccentricities of the vertices is expressed in the ascending order and the multiplicity is expressed as superscript.

We now define and represent the mean, median and mode of eccentricities of the vertices of a graph with certain symbols.

Definition 1.1 The **mean eccentricity** or average eccentricity is denoted by $\mu_{me}(G)$.

Definition 1.2 The **median eccentricity** is defined as the value which is in the middle of the eccentric sequence and is denoted by $\mu_{md}(G)$.

Definition 1.3 The **mode eccentricity** is defined as the value which is most repeated in the eccentric sequence and is denoted by $\mu_{mo}(G)$.

Definition 1.4 The graphs having same mean, median and mode eccentricities are characterized into a new family called μ-graph. The central value $e_{\mu}(G)$of a μ-graph is defined by $e_{\mu}(G) = \mu_{me}(G) = \mu_{md}(G) = \mu_{mo}(G)$.

Mean Eccentricity	$\mu_{me}(G)$
Median Eccentricity	$\mu_{md}(G)$
Mode Eccentricity	$\mu_{mo}(G)$

2. $\mu_{me}(G), \mu_{md}(G)$ and $\mu_{mo}(G)$ OF SOME STANDARD GRAPHS

We discuss the mean eccentricity, median eccentricity and mode eccentricity of path, cycle, wheel, hypercube and Hajȯs graph.

Theorem 2.1 [2] The mean eccentricity $\mu_{me}(G)$ of a path P_n is

$$\mu_{me}(P_n) = \begin{cases} \dfrac{(n-1)(3n-1)}{4n} & if\ n\ is\ odd \\ \dfrac{3n-2}{4} & if\ n\ is\ even \end{cases}$$

Theorem 2.2 The median eccentricity $\mu_{md}(G)$ of a path P_n is

$$\mu_{md}(P_n) = \begin{cases} \left\lceil \dfrac{3n-2}{4} \right\rceil, if\ n \equiv 3 (\mathrm{mod}\ 4) \\ \left\lfloor \dfrac{3n-2}{4} \right\rfloor, else \end{cases} \quad (1)$$

Proof: Let P_n be a path with the vertex set $V(P_n)=\{v_1, v_2, \dots, v_n\}$. $v_i\ and\ v_j$ are adjacent if and only if $j = i+1, 1 \le i \le n-1\ and\ 2 \le j \le n$. We can see that the eccentricities of $v_i\ and\ v_{n+1-i}, 1 \le i \le n,$ are equal. For a path the highest eccentricity, $n-1$, is for $v_1 and\ v_n$. All the eccentricities appear in pairs from $n-1\ to\ \frac{n}{2}$ if n is even. If n is odd, the eccentricities from $n-1\ to\ \frac{n+1}{2}$ appear in pairs and the vertex $v_{\frac{n+1}{2}}$ alone will have the eccentricity $\left\lfloor \frac{n}{2} \right\rfloor$. Obviously, the median eccentricity is one of the values in the eccentric sequence. Therefore, we need to show that the value in equation**Error! Reference source not found.** appears in eccentric sequence of a path P_n. In addition to these, we are aware that, there are $\left\lfloor \dfrac{n}{2} \right\rfloor$ distinct terms in the eccentric sequence. The eccentric sequence of the path P_n for an odd n is

$$\left\lfloor \frac{n}{2} \right\rfloor, \left(\left\lfloor \frac{n}{2} \right\rfloor + 1 \right)^2, \left(\left\lfloor \frac{n}{2} \right\rfloor + 2 \right)^2, \left(\left\lfloor \frac{n}{2} \right\rfloor + 3 \right)^2, \ldots, (n-1)^2 \quad (1)$$

Similarly, for even *n*, the eccentric sequence is

$$\left(\frac{n}{2}\right)^2, \left(\frac{n}{2}+1\right)^2, \left(\frac{n}{2}+2\right)^2, \left(\frac{n}{2}+3\right)^2, \ldots, (n-1)^2 \quad (2)$$

We prove the result by analysing the divisibility of n by 4.

Case 1: $n \equiv 0 \pmod 4$

Let $n = 4k$ for some non-negative integer *k*. The largest eccentricity 4*k*-1 is for the end vertices v_1 and v_{4k}. Since *n* is even, the smallest eccentricity 2k is for the vertices v_{2k} and v_{2k+1}. Arranging $2k=\frac{n}{2}$, to 4*k*-1=*n*-1, we obtain the median value as 3*k*-1. Since n=4*k*, we have 3*k*-1= $\frac{3n}{4} - 1$. However, this is same as $\left\lfloor \frac{3n-2}{4} \right\rfloor$, when *n*=4*k* for every non-negative integer *k*.

Case 2: $n \equiv 1 \pmod 4$

Let $n = 4k+1$. Then, the largest eccentricity 4*k* is for the vertices v_1 and v_{4k+1} and the smallest eccentricity 2*k*+1 is for the vertex v_{2k+1}. All eccentricities from 4*k* to 2*k*+2 appear twice and the eccentricity 2*k*+1 appears only once. Arranging all the 4*k*+1 eccentricities in the ascending order, we get the median value as 3*k*. Since n=4*k*+1, we have 3*k* = $\frac{3n-3}{4}$. However, this is same as $\left\lfloor \frac{3n-2}{4} \right\rfloor$, when *n*=4*k*+*1* for every non-negative integer *k*.

Case 3: $n \equiv 2 \pmod 4$

Let $n = 4k+2$. In this case, the eccentricities are from 2*k*+1 to 4*k*+1, all appearing twice each. After arranging in the ascending order we get the median value as 3*k*+2. Since n=4*k*+*2*, we have 3*k*+1= $\frac{3n-2}{4}$. However, this is same as $\left\lfloor \frac{3n-2}{4} \right\rfloor$, when *n*=4*k*+*2* for every non-negative integer *k*.

Case 4: $n \equiv 3 \pmod 4$ eccentricity

Let $n = 4k+3$ for some non-negative integer *k*. The eccentricities are 4*k*+2 to 2*k*+2 appearing twice and 2*k*+1 appearing just once. Arranging the eccentricities in the ascending order, we get the median value as 3k+2. Since n=4*k*+*3*, we have 3*k*+2= $\frac{3n-1}{4}$. However, this is same as $\left\lfloor \frac{3n-2}{4} \right\rfloor$, when *n*=4*k*+*3* for every non-negative integer *k*. Hence we have the proof.

Theorem 2.3 The mode eccentricity μ_{mo} of a path P_n is

$$\mu_{mo}(P_n) = \left\{ \left(\frac{n}{2}\right), \left(\frac{n}{2}+1\right), \left(\frac{n}{2}+2\right), \ldots, \left(n-1\right) \right\}$$

Proof: The proof is trivial since the eccentricities of a path appear in pairs and from equations (1) and(2).

In the next theorem, we prove that the centrality measures of a cycle are equal.

Theorem 2.4 The mean eccentricity (μ_{me}), median eccentricity (μ_{md}) and mode eccentricity (μ_{mo}) of a Cycle C_n is $\mu_{me}C_n = \mu_{md}C_n = \mu_{mo}C_n = \left\lfloor \frac{n}{2} \right\rfloor$

Proof: The proof is trivial. The eccentricities of vertices in a cycle C_n are equal and

$$e_G(C_n) = \begin{cases} \frac{n}{2} & \text{if n is even} \\ \left\lfloor \frac{n}{2} \right\rfloor & \text{if n is odd} \end{cases}$$

Hence we obtain the result.

The definition of a wheel W_n, holds that one vertex will have eccentricity as one and the remaining *(n - 1)* vertices will have eccentricity two. Thus we have the following theorem.

Theorem 2.5 The mean eccentricity (μ_{me}), median eccentricity (μ_{md}) and mode eccentricity (μ_{mo}) of a Wheel W_n, is $\mu_{me}(W_n) = \frac{2n-1}{n}$ and $\mu_{md}(W_n) = \mu_{mo}(W_n) = 2$

Proof: In a wheel W_n, the eccentricity of the central vertex is always one since it is adjacent to all other vertices. Remaining (n - 1) vertices will have 2 as eccentricity. Thus the mean eccentricity is given by

$$\begin{aligned} \mu_{me}(W_n) &= \frac{1}{n} \sum_{v \grave{o} V(W_n)} e_{W_n}(v) \\ &= \frac{1}{n}\left[1 + 2(n-1)\right] \\ &= \frac{2n-1}{n}. \end{aligned}$$

The median eccentricity (μ_{md}) and mode eccentricity (μ_{mo}) of a wheel W_n is always two. Hence we have $\mu_{md}(W_n) = \mu_{mo}(W_n) = 2$.

The hypercube Q_n has the same diameter, thus we conclude saying

Theorem 2.6 The mean eccentricity (μ_{me}), median eccentricity (μ_{md}) and mode eccentricity (μ_{mo}) of a hypercube Q_n is $\mu_{me}(Q_n) = \mu_{md}(Q_n) = \mu_{mo}(Q_n) = n$.

Proof: The diameter of a hypercube is n, since it takes *n* steps to change all *n* coordinates. Thus its mean eccentricity (μ_{me}), median eccentricity (μ_{md}) and mode eccentricity (μ_{mo}) are one and the same. Hence, the proof.

For all self-centered graphs, we obtain the mean eccentricity, median eccentricity and mode eccentricity in the following theorem.

Theorem 2.7 The mean eccentricity (μ_{me}), median eccentricity (μ_{md}) and mode eccentricity (μ_{mo}) of a self-centered graph is $\mu_{me}(G) = \mu_{md}(G) = \mu_{mo}(G) = e_G(v)$.

Proof. A self-centered graph has r(G) = diam(G). Hence every vertex of G has the same eccentricity. Hence, the proof.

Remark 2.8 All regular graphs - cycle graph, complete graph, k-partite, Petersen graph, dodecahedral graph, etc., are having the same mean eccentricity (μ_{me}), median eccentricity (μ_{md}) and mode eccentricity (μ_{mo}), since they are self-centered graphs.

Theorem 2.9 The mean eccentricity (μ_{me}), median eccentricity (μ_{md}) and mode eccentricity (μ_{mo}) of a Hajǒs graph (S_n) is $\mu_{me}(S_n) = \mu_{md}(S_n) = \mu_{mo}(S_n) = 2$

Proof: The sun graph S_n is constructed as the complete graph K_n with an outer ring of n vertices, of which each vertex is joined to both endpoints of the closest outer edge of the complete graph. Then 3-sun S_3, the eccentricity of each six vertices is two. Then $e_\mu(S_3) = \mu_{me}(S_3) = \mu_{md}(S_3) = \mu_{mo}(S_3) = 2.$

Hence Hajǒs graph is a μ -graph.

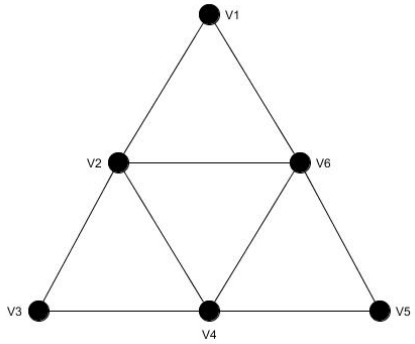

Fig1: 3-Sun Graph (Hajǒs graph)

3. THE μ-GRAPH

In this section we define a new family of graphs as μ -Graph with the property of equal mean eccentricity (μ_{me}), median eccentricity (μ_{md}) and mode eccentricity (μ_{mo}).

Definition 3.1 A μ -graph is a graph, if for any graph G, μ_{me} (G) = μ_{md} (G) = μ_{mo} (G) on the set of eccentricities of the vertices of a given graph.

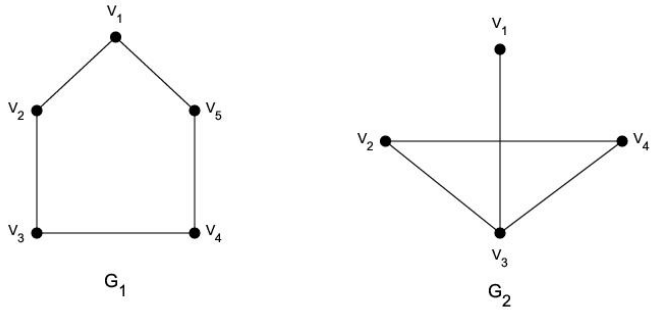

Fig 2: G_1 is a μ -graph & G_2 is not a μ -graph

Example 3.2 In Figure 2, the eccentric sequence of G_1 is 2^5. Therefore, $\mu_{me}(G_1)$ = $\mu_{md}(G_1)$ = $\mu_{mo}(G_1)$. Hence G_1 is a μ - *graph*. But G_2 in Figure 2, G_2 is not a $\mu-$graph. The eccentric sequence of G_2 is 1, 2^3. Therefore, $\mu_{me}(G_2) \neq \mu_{md}(G_2) = \mu_{mo}(G_2)$. The measures of centrality tend to a value which is central to all values. Similarly, in graph, we find the vertex or vertices which is/are central. In a $\mu-$graph, we define a central value by the following definition. All the vertices having this central value as the eccentricity would be the central vertices.

Definition 3.3 The *central value* $e_\mu(G)$ of a $\mu-$graph is defined by $e_\mu(G) = \mu_{me}(G) = \mu_{md}(G) = \mu_{mo}(G).$

The characterisation of Path is given in the next theorem.

Theorem 3.4 Path P_n is a μ-graph if and only if n is twice any positive odd number.

Proof: We prove the necessary and sufficient condition for path to be a μ - graph. Let P_n be a $\mu-$graph. By the definition of $\mu-$graph, we have

$$e_\mu(P_n) = \mu_{me}(P_n) = \mu_{md}(P_n) = \mu_{mo}(P_n) \tag{3}$$

To prove: if P_n is a $\mu-$graph, then $n = 2(2k+1)$, $\forall k \in W$. We know from theorem 2.1 that

$$\mu_{me}(P_n) = \begin{cases} \dfrac{(n-1)(3n-1)}{4n} & \text{if n is odd} \\ \dfrac{3n-2}{4} & \text{if n is even} \end{cases} \tag{4}$$

For all values of *n*, from theorem 2.2, we have median eccentricity as

$$\mu_{md}(P_n) = \frac{3n-2}{4} \tag{5}$$

The value of mode eccentricity by theorem 2.3 becomes

$$\mu_{mo}(P_n) = e_{P_n}(v_i) \tag{6}$$

Equation (6) exhibits the mode eccentricity as one of the values in the eccentric sequence. From equations (4) and (5), only for even $n \in N$, the equation (3) satisfied. Hence from equations(3),(4), (5) and (6), we get

$$e_{\mu}(P_n) = \frac{3n-2}{4} \tag{7}$$

The equation (7) is true only for $n = 2,6,10,14,18,.....$ Thus $n = 2(2k+1)$ where $k \in W$. Hence if P_n is a $\mu-$graph, then $n = 2(2k+1)$, where $k \in W$.

Conversely, we prove that if $n = 2(2k+1)$, then P_n is a $\mu-$graph. We prove the converse part using mathematical induction on *k*.

When $k = 0$, *n* becomes 2. Obviously, P_2 is a μ-graph. Hence the result is true if $k = 0$. Assume for $k = m$, the result is true. Then $n = 2(2m+1)$ and P_{4m+2} is a μ-graph.

To verify that the result is true for $k = m+1$. This implies that $n = 2(2(m+1)+1) = 2(2m+1)+4$. By the induction hypothesis, for $n = 2(2m+1)$, P_n is a μ-graph. We need to show that it is true for $n = 2(2m+1)+4$.

For this *n,* the corresponding path is P_{4m+6}. The path P_{4m+6} has four vertices more than path P_{4m+2}.

Using equation (2), the eccentric sequence becomes $(2m+3)^2,(2m+4)^2,...,(4m+5)^2$.

Using theorem 2.1, we get the mean eccentricity as

$$\mu_{me}(P_{4m+6}) = 3m+4 \tag{8}$$

Similarly using theorem 2.2, we obtain the median eccentricity as

$$\mu_{md}(P_{4m+6}) = 3m+4 \tag{9}$$

We know that eccentricities of the vertices of an even path come in pairs. Thus mode eccentricity of a path is

$$\mu_{mo}(P_n) = e_{P_n}(v_i) \tag{10}$$

From equations (8), (9) and (10), we conclude that $e_{\mu}(P_n) = \mu_{me}(P_n) = \mu_{md}(P_n) = \mu_{mo}(P_n)$.

Hence P_{4m+6} is a μ-graph. Therefore the result is true for *k = m + 1*. Hence by induction, it is true for all *k*. Thus for $k \in$ W, $n = 2(2k+1)$, P_n is a μ-graph. Hence the proof.

Theorem 3.5 A graph G is self-centered then it is a μ-graph.

We prove that if G is a self-centered graph, then G is a μ-graph.

By definition, self-centered graphs have $r(G) = diam(G)$. Thus all the vertices have the same eccentricity. From theorem 2.7, we conclude that the mean eccentricity, median eccentricity and mode eccentricity of the self-centered graph are the same. Hence all self-centered graphs are μ -graphs.

Thus, if G is a path P_n, n = 2(2k + 1), where k $\in$ W, the set of whole numbers or G is a self-centered graph, then G is a μ -graph.

4. THE CENTRAL VALUE ($e_\mu(G)$) OF SOME STANDARD GRAPHS

Here we discuss the central value of path, *k*-regular graphs and *k*-partite graphs.

Corollary 4.1 The *central value* of P_n for $n = 2(2k+1)$ is $e_\mu(P_n) = \frac{3n-2}{4}$, where $k \in W$.

Proof: It is clear that when $n = 2(2k+1)$, the path P_n is a μ-graph. From theorems 2.1, 2.2 and 2.3, we conclude that $e_\mu(P_n) = \frac{3n-2}{4}$, where $k \in W$.

Corollary 4.2 The central value of a *k*-regular graph is

$$e_\mu(G) = \begin{cases} 1 & \text{if } k = n-1 \\ 2 & \text{if } \frac{n}{2}-1 \le k < n-1 \text{ for all even } n. \\ \left\lfloor \frac{n}{k} \right\rfloor & \text{if } 2 \le k < \frac{n}{2}-1 \end{cases}$$

Cycle, hypercube, Petersen graph and 3-Sun graph or Hajȯs graph all belong to *k*-regular graphs.

Corollary 4.3 The *central value* of $K_{p,q,\ldots,r}$ is $e_\mu(K_{p,q,\ldots,r}) = k$

5. BOUNDS OF CENTRAL VALUE OF A GRAPH

Theorem 4.4 For any simple, finite and connected graph G with n $\geq$ 2 vertices,

$$1 \le e_\mu(G) \le \frac{3n-2}{4} \qquad (11)$$

Proof: We know that if e_μ (G) = 1, then eccentricities of each of the vertices is one. Then the given graph is a complete graph K_n. Hence the lower bound holds true.

Next, we consider the upper bound for both cyclic and acyclic graphs.

Case 1: Let G be an acyclic graph. Since G is connected, it is a tree. Among all trees of n vertices, path have the maximum eccentricity *n–1*. Hence we obtain, $e_G(v) = n-1 \quad \text{for } v \in V(G)$. From Corollary 4.1, we know that $e_\mu(P_n) = \frac{3n-2}{4}$.

Hence for acyclic graph G, the equality of the upper bound is attained.

Case 2: Let G be a cyclic graph. Cyclic graphs may be unicyclic or multi-cycle graph. If the graph G is unicyclic of n vertices, then the maximum eccentricity we can obtain could be *n - 2*. Still the upper bound holds in equation(11). With the increase in the edges of n vertices graph, the eccentricity reduces. This is also the case with multi-cycle graphs.

Hence, $1 \leq e_{\mu}(G) \leq \frac{3n-2}{4}$ for $n \geq 2$.

6. CONCLUSION

In this paper, we have extended the study of the centrality parameters of eccentricity of graphs. We characterized the graphs of identical mean eccentricity, median eccentricity and mode eccentricity. The sufficient condition for a graph to be a μ-graph is proved. The concept of central values of a μ-graph is defined and investigated for certain standard graphs. The study could be extended in finding the necessary condition for a graph to be a μ-graph.

7. REFERENCES

[1] F. Buckley and F. Harary, Distance in Graphs, Addison-Wesley, Redwood City, (1990).

[2] P. Dankelmann, W. Goddard and C. S. Swart, "The Average Eccentricity of a Graph and Its Subgraphs, Utilitas Mathematica, 65 (2004) 41-51.

[3] P. Hage and F. Harary, Social Network, 17 (1995) 57.

[4] F. Harary, Graph Theory, Addison-Wesley, Reading, (1969).

[5] J. S. Kauffman, Mode Vertices and Mode Graphs, M.S. thesis, Dept. Math., East Tennessee State University, (2000).

[6] S. Mukambi and S. D. Hove-Musekaw, Indian J. Pure Appl. Math., 43 (2012) 637.

PK ISSN 0022- 2941; CODEN JNSMAC
Vol. 57, (2017) PP 10-18

POWER SERIES VARIATIONAL ITERATION METHOD FOR THE NUMERICAL TREATMENT OF FIFTH ORDER BOUNDARY VALUE PROBLEMS

EBIMENE J. MAMADU[1] AND IGNATIUS N. NJOSEH[2]

[1]Department of Mathematics, University of Ilorin, P.M.B 1515, Ilorin, Nigeria
[2]Department of Mathematics, Delta State University, Abraka, Nigeria
Email: mamaduebimene@hotmail.com[1], njoseh@delsu.edu.ng[2]

ABSTRACT

In this paper, we considered the numerical treatment of the fifth order boundary value problem (BVP) through an elegant mixture of the power series approximation method (PSAM) and the Variational iteration method (VIM). The method approximates the analytic solution using a rapid convergent power series which satisfies the given boundary conditions; thus giving rise to the initial approximation. The method was tested on both linear and nonlinear fifth order boundary value problems with known analytic solutions. Results obtained were presented both graphically and in tables. All computational analysis in this work was performed with Maple 18 software.

Keywords: Boundary value problem, power series, trial solution, Lagrange multiplier, approximate solution.

1. INTRODUCTION

Let us consider a general fifth order boundary value problem

$$y^{(5)}(x) = r(x)y(x) + f(x), 0 < x < 1 \quad (1)$$

subject to the boundary conditions

$$y(0) = A_0, y'(0) = A_1, y"(0) = A_2, y(1) = B_0, y'(1) = B_1, \quad (2)$$

where $f(x), y(x)$, and $r(x)$ are assumed real and continuous on $[0,1]$, A_i, $i = 0(1)2$, and $B_i, i = 0,1$, are finite real constants in $[0,1]$.

These types of equations are very useful in science and technology, especially in the field of mathematical modelling. However, solving these equations analytically proves difficult and strenuous due to complex algorithm involved. Hence, many researchers instead prefer seeking their approximate solutions. In recent years, various numerical methods have been developed and implemented by researchers, some of these include: the power series approximation method (PSAM) [1], orthogonal collocation

approach [2], Galerkin method [3], Tau-collocation method [4], weighted residual method [5], homotopy perturbation method (HPM) [6], variational iteration method [7-8], Adomian decomposition method [9-10], optimal homotopy asymptotic method (OHAM) [11], differential transform method (DTM) [12] etc. In like manner, [13] considered a coupling method involving the Sumudu transform and the variational iteration method for a class of local fraction diffusion equation, while [14] considered an elegant mixture of the series expansion method and the variational iteration method to the Helmholtz equation involving local fractional derivation operators. The Laplace transforms and the variational iteration method has been applied for solving linear partial differential equations with local fractional derivative [15]. Furthermore, a local fractional variational iteration algorithm has been developed to solve problems such as the Fokker-Planck equation on a cantor set, and the non-homogeneous model associated with non-differentiable heat flow [16-17].

In this paper, we aim at solving the fifth order boundary value problem using power series variational iteration method (PSVIM). The PSVIM comprises of the PSAM (developed by Njoseh and Mamadu [1] for a generalized nth order boundary value problem) and the variational iteration method (developed by He [8]). In this method, the PSAM is employed to seek the initial approximation via the trial solution satisfying the given boundary conditions. The correction functional is constructed and the Lagrange multiplier is estimated via variational theory to start iteration. The method approximates the analytic solution using a rapid convergent power series (trial function) with no regard to linearization or perturbation.

2. BASIC IDEAS OF POWER SERIES VARIATIONAL ITERATION METHOD

PSAM requires transforming the set of equations (1) - (2) into system of ordinary differential equations [1]

$$y = y_1, \frac{dy_1}{dx} = y_2, \frac{dy_2}{dx} = y_3, \frac{dy_3}{dx} = y_4, \ \frac{dy_4}{dx} = y_5 = f(x) + \alpha(x)y(x), \tag{3}$$

subject to the conditions in (2).

We consider the theorem below:

Theorem 1.1

Using PSAM, the approximate solution to (1) is given as

$$y(x) = \sum_{i=0}^{\frac{n-1}{2}} y^{(i)}(x)x^i, \ y^{(i)}(x) = \frac{A_i}{i!} \tag{4}$$

subject to

$$y(0) = A_0, y^{(1)}(0) = A_1, y^{(2)}(0) = A_2, y^{(3)}(0) = A_3, y^{(4)}(0) = A_4 \tag{5}$$

Proof:

Let the approximate solution be given as

$$y(x) = \sum_{i=0}^{n-1} y^{(i)}(x)x^i \tag{6}$$

Hence, substituting (6) into (4), and using the prescribed boundary at $x = 0$, we have

$$y(x) = y^{(1)}(x) + i\sum_{i=2}^{n-1} y^i(x)x^{i-1}, \tag{7}$$

But, $y^{(1)}(0) = A_1$, which implies

$$y(x) = A_1 + i\sum_{i=2}^{n-1} y^i(x)x^{i-1} \tag{8}$$

Similarly,

$$y(x) = 2y^{(2)}(x) + i(i-1)\sum_{i=3}^{n-1} y^{(i)}(x)x^{i-2}.$$

$$\Longrightarrow y(x) = A_2 + i(i-1)\sum_{i=3}^{n-1} y^i(x)x^{i-2},$$

where $y^{(2)}(x) = \frac{A_2}{2!}$.

Continuing this process, we arrive at

$$y^{(i)}(x) = \frac{A_i}{i!},\ i \geq 0. \tag{9}$$

Thus,

$$y(x) = \sum_{i=0}^{n-1} \frac{A_i}{i!}x^i \tag{10}$$

Now, for $n = 5$ in (4), we have

$$y(x) = y(0) + y^{(1)}(0)x + \frac{y^{(2)}(0)}{2}x^2 + \frac{y^{(3)}(0)}{6}x^3 + \frac{y^{(4)}(0)}{24}x^4 \tag{11}$$

subjecting (11) to (5), we have that

$$y(x) = A_0 + A_1x + \frac{A_2}{2}x^2 + \frac{A_3}{6}x^3 + \frac{A_4}{24}x^4 \tag{12}$$

which is equivalent to the initial approximation.

Thus, the PSAM is employed here in estimating the initial approximation by subjecting the approximate solution (4) to the prescribed boundary conditions at $x = 0$.

Remark 1:

Equation (4) is equivalent to the initial approximation as earlier stated. This approximation is however obtained at the boundary $x = 0$. From (2), we are given the following boundary conditions at $x = 0$,

$$y(0) = A_0, y^{(1)}(0) = A_1, y^{(2)}(0) = A_2$$

which are inadequate or insufficient with regard to the order of the boundary value problem. Thus, we define

$$y^{(3)}(0) = A_3, y^{(4)}(0) = A_4$$

so as to correspond to the order of the BVP.

The parameters A_0, A_1, A_2 are given; while A_3 and A_4 are unknowns which are computed at the boundary $x = 1$ in equation (2).

Having obtained the initial approximation, we next apply the variational iteration method.

The variational iteration method requires the construction of a correction functional for equation (1) subject to the conditions in (2) [7]

$$y_{n+1}(x) = y_n(x) + \int_0^x \lambda(s)\left(\frac{d^5}{ds^5}y_n(s) - r(s)y_n(s) - f(s)\right)ds, n \geq 0,$$

(13)

where $\lambda(s)$ is the general Lagrange multiplier, which can be obtained optimally via variational theory and $\tilde{y}_n(s) = 0$. The Lagrange multiplier, $\lambda(s)$ can be obtained using the formula in [8]

$$\lambda_n(s) = (-1)^n \frac{(s-x)^{(n-1)}}{(n-1)!} \tag{14}$$

where n is the order of the derivative.

Hence, the PSVIM for (1) becomes

$$y_0(x) = A_0 + A_1 x + \frac{A_2}{2}x^2 + \frac{A_3}{6}x^3 + \frac{A_4}{24}x^4 \tag{15}$$

$$y_{n+1}(x) = y_n(x) + \int_0^x \lambda(s)\left(\frac{d^5}{ds^5}y_n(s) - r(s)y_n(s) - f(s)\right)ds, n \geq 0 \tag{16}$$

for the computation of

$$y_n(x), n \geq 1.$$

The unknowns in each iterate are computed at $x = 1$.

3. ERROR ANALYSIS AND CONVERGENCE THEOREM

Let

$$e_n(x) = y(x) - y_n(x) \tag{17}$$

be an error function of the approximate solution $y_n(x)$ to the exact solution $y(x)$.

This implies that $y_n(x)$ satisfies

$$y_n^{(5)}(x) = r(x)y(x) + f(x) + H_n(x), 0 < x < 1 \tag{18}$$

subject to the boundary conditions

$$y^{(m)}(0) = A_m, m = 0,1,2 \tag{19}$$

$$y^{(m)}(1) = B_m, m = 0,1 \tag{20}$$

$H_n(x)$ in equation (18) is called the perturbation term, and is given as$H_n(x) =$

$$y_n^{(5)}(x) - r(x)y(x) - f(x) \tag{21}$$

Transforming the set of equations (18)-(20) and finding an approximant $e_n^{(5)}(x)$ to the error function $e_n(x)$,

the error function therefore satisfies

$$H_n(x) = r(x)y(x) + f(x) - y_n^{(5)}(x),\ 0 < x < 1,$$

with conditions

$$y^{(m)}(0) = 0, \qquad m = 0,1,2.$$

$$y^{(m)}(1) = 0, \ \ m = 0,1.$$

Lemma 1.1. (Sufficient Conditions of Convergence) [7]

Define $y^5(x)$ by D(u) in (1) such that $D(u) = r(x)y(x) + f(x)$. Then, (16) converges if the following conditions are satisfied:

i. $(D(u) - D(v), u - v) \leq \tau\|u - v\|^2, \tau > 0, u, v \in H$

ii. For $\Omega > 0$, there exist $I(\Omega) > 0$ such that $\|u\| \leq \Omega,\ u, \in H$, then

$(D(u) - D(v), u - v) \leq I(\Omega)\|u - v\|\|r\|, r \in H.$

where $H = ((a, b) \times [0, T]$ is a Hilbert Space.

Lemma 1.2. [18]

Suppose that the boundary value problem (1) satisfy the condition in Lemma (1.1), and $y(x), y_n(x) \in C^5[0,1],\ n = 1,2,\cdots.$ then the sequence $\{y_n(x)\}_{n=1}^{\infty}$ defined by (16) converges to the solution of (1).

Theorem 1.2

Given

$$y(x) = \sum_{i=0}^{\frac{n-1}{2}} \frac{A_i}{i!} x^i,$$

where $y^{(m)}(0) = A_m,\ m = 0,1,2,3,4.$ The PSVIM for the considered boundary value problem (1) and (2) converges as $n \to \infty$.

Proof:

Let the approximate solution be given as

$$y(x) = \sum_{i=0}^{n-1} y^{(i)}(0) x^i,$$

then for $i \geq 0$, we have that

$$y(x) = \sum_{i=0}^{n-1} \frac{A_i}{i!} x^i \ ,$$

which evidently is the initial approximation as shown in section 2 of this work.

Since, the considered boundary value problem is of order 5, then

$$y_0(x) = \sum_{i=0}^{4} \frac{A_i}{i!} x^i.$$

By the theorem of VIM [7-8],

$$y_{n+1}(x) = y_n(x) + \int_0^x \frac{(s-x)^4}{24} \left(\frac{d^5}{ds^5} y_n(s) - r(s) y_n(s) - f(s) \right) ds, n \geq 0.$$

When $n = 0$:

$$y_1(x) = y_0(x) + \int_0^x \frac{(s-x)^4}{24} \left(\frac{d^5}{ds^5} y_0(s) - r(s) y_0(s) - f(s) \right) ds.$$

When $n = 1$:

$$y_2(x) = y_1(x) + \int_0^x \frac{(s-x)^4}{24} \left(\frac{d^5}{ds^5} y_1(s) - r(s) y_1(s) - f(s) \right) ds.$$

$$\vdots$$

$$y_n(x) = y_{n-1}(x) + \int_0^x \frac{(s-x)^4}{24} \left(\frac{d^5}{ds^5} y_{n-1}(s) - r(s) y_{n-1}(s) - f(s) \right) ds, n \geq 1.$$

Thus, by Lemmas (1.1) and (1.2), the approximate solution $y_n(x)$ converges to the exact solution $y(x)$ as $n \to \infty$.

4. NUMERICAL EXAMPLES

To demonstrate the accuracy of the method, we consider two boundary value problems of fifth order with known analytic solution. All numerical results are obtained using Maple 18 software.

Example 4.1. [19]

Consider the following nonlinear boundary value problem of fifth order,

$$y^{(v)}(x) = e^{-x} y^2(x) \tag{22}$$

Subject to the boundary conditions

$$y(0) = 1, y'(0) = 1, y''(0) = 1, y(1) = y'(1) = e$$

The exact solution is

$$y(x) = e^x.$$

Applying the methodology in section 2, we have,

$$y_0(x) = 1 + x + \frac{1}{2}x^2 + \frac{A_3}{6}x^3 + \frac{A_4}{24}x^4 \quad (23)$$

$$y_{n+1}(x) = y_n(x) - \int_0^x \frac{(s-x)^4}{4!}\left(\frac{d^5}{ds^5}y_n(s) - \left(1 - s + \frac{1}{2}s^2 - \frac{1}{3!}s^3 + \frac{1}{4!}s^4\right)y_n^2(s)\right)ds, n \geq 0 \quad (24)$$

Solving equation (24) for $n \geq 0$, and estimating A_3 and A_4 at the boundary at $x = 1$, we generate the following error bound for each iterate as shown in **Table 1** below.

The approximations for $y_n(x), n = 0,1,\cdots$, are given as

$$y_0(x) = 1 + x + \frac{1}{2}x^2 + 0.1548455000x^3 + 0.06343633333x^4.$$

$$\begin{aligned} y_1(x) = \quad & 1 + x + \frac{1}{2}x^2 + 0.1666685000x^3 + 0.04166470833x^4 + 0.008333333333x^5 \\ & + 0.00138888889x^6 + 0.000198412704x^7 + 0.000024802122x^8 \\ & + 0.0000027554352x^9 \\ & + 2.5052264E-07x^{11} + 1.4613888E-07x^{12} + 5.620690E-08x^{13} \\ & + 1.686217E-08x^{14} \\ & + 4.014581E-09x^{15} + 5.5204110E-10x^{16} + 9.7407910E-011x^{17}. \end{aligned}$$

$$\vdots$$

Table 1. Estimates of A_3 and A_4 with the maximum error for each iterate for Example 4.1.

	A_3	A_4	Maximum Error
$y_0(x)$	0.929073	1.522472	9.7290E-06
$y_1(x)$	1.000011	0.999953	1.9385E-09
$y_2(x)$	1.000033	0.999849	4.0000E-00

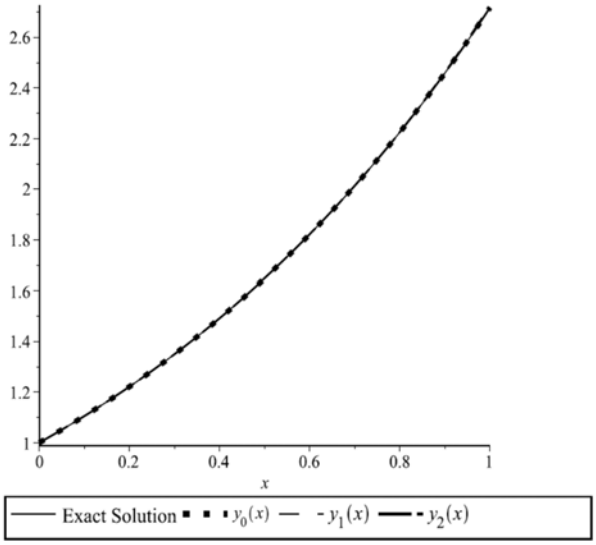

Figure 1: The comparison of each iterate and the exact solution for Example 4.1.

Example 4.2. [19]

Consider the linear boundary value problem of fifth order

$$y^{(v)}(x) = y - 15e^x - 10xe^x \quad (25)$$

Subject to the boundary conditions

$$y(0) = 0, y'(0) = 1, y''(0) = 0, y(1) = 0, y'(1) = -e$$

The exact solution is

$$y(x) = x(1-x)e^x$$

By the methodology in section 2, we have,

$$y_0(x) = x + \frac{A_3}{6}x^3 + \frac{A_4}{24}x^4 \quad (26)$$

$$y_{n+1}(x) = y_n(x) - \int_0^x \frac{(s-x)^4}{4!}\left(\frac{d^5}{ds^5}y_n(s) - y_n(s) + (15+10s)\left(1 - s + \frac{1}{2}s^2 - \frac{1}{3!}s^3 + \frac{1}{4!}s^4\right)\right)ds, n \geq 0 \quad (27)$$

Solving equation (27) for $n \geq 0$, and estimating A_3 and A_4 at the boundary $x = 1$, we obtain the following error bound for each iterate as shown in **Table 2** below.

The approximations for $y_n(x), n = 0,1,\cdots$, are given as

$$y_0(x) = x - 0.2817181667x^3 - 0.7182818333x^4.$$

$$\begin{aligned} y_1(x) = \; & x - 0.4999308333x^3 - 0.3334135833x^4 - 0.1250000000x^5 \\ & + 0.0083333334x^6 \\ & + 0.00099206346x^7 - 0.00044641832x^8 + 0.0000046842118x^9 - \\ & 0.000013778666x^{10}. \end{aligned}$$

Table 2. Estimates for A_3 and A_4 with the maximum errors for each iterate for Example 4.2.

	A_3	A_4	Maximum Error
$y_0(x)$	-1.690309	-17.238764	1.8107E-04
$y_1(x)$	-2.999585	-8.001926	6.1200E-08
$y_2(x)$	-2.999763	-8.001098	3.4960E-08

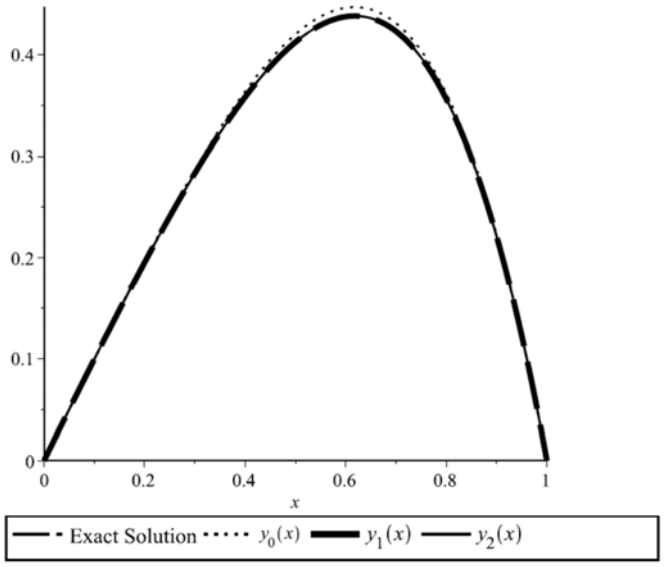

Figure 2: The comparison of each iterate and the exact solution for Example 4.2.

5. DISCUSSION OF RESULTS

The numerical evidences show that the approximate solution (broken lines) converges favourably to the exact solution (solid lines) as shown in the **figure 1** and **2** with maximum errors of **1.9385E-09** and **6.1200E-08** for **Example 4.1** and 4.**2** respectively. This implies that with few iterations the approximate solution will converge absolutely to the exact solution.

6. CONCLUSION

We have implemented the PSVIM on linear and nonlinear fifth order boundary value problems. The method is explicit and accurate as the numerical results reveal with no requirement for linearization or perturbation. The method can be extended to other problems such as random processes problems.

REFERENCES

1. I. N. Njoseh and E. J. Mamadu, Applied Mathematics, 7 (2016) 1215.
2. A. S. Olagunju and F. L. Joseph, IOSR Journal of Mathematics, 7(2) (2013) 42.
3. M. B. Hossain and M. S. Islam, Dhaka Univ. J. Sci., 62(2) (2014) 101.
4. E. J. Mamadu and I. N. Njoseh, Journal of Applied Mathematics and Physics, 4 (2016) 383.
5. R. A. Oderinu, Gen. Math. Notes, 24(1) (2014) 17.
6. M. Grover and K. T. Arun, International Journal of Computational Mathematics and Numerical Simulation, 4(1) (2011) 99.
7. E. J. Mamadu and I. N. Njoseh, Transactions of the NAMP., 2 (2016) 65.
8. S. Abbasbandy and E. Shivanian, Mathematical and Computational Applications, 14(2) (2009) 147.
9. G. Adomian, Solving frontier problems of Physics: The Decomposition Method, Springer (1994).

10. G. Adomian and R. Rach, Comput. Math. Appl., 24 (1992) 61.

11. J. Ali, S. Islam, T. M. Rahim and G. Zaman, World Applied Sciences Journal, 11(3) (2010) 371.

12. S. Islam, S. Haq and J. Ali, Commun Nonlinear Sci Numer Simulat.,14 (2009) 1132.

13. F. Gao, H. M. Srivastava, Y. Gao and X. Yang, Journal of Nonlinear Science and Applications, 9 (2016) 5830.

14. A. Yang, Z. Chen, H. M. Srivastava, and X. Yang, Abstract and Applied Analysis, 2013 (2013) 1-6.

15. A. Yang, J. Li, H. M. Srivastava, G. Xie and X. Yang. Discrete Dynamics in Nature and Society, 2014 (2014) 1-8.

16. D. Baleanu, H. M. Srivastava and X. Yang, Progress in Fractional Differentiation and Application, 1(1) (2015) 1-11.

17. Y. Zhang, H. M. Srivastava and M. C. Baleanu, Advances in Mechanical Engineering, 7(10) (2015) 1.

18. H. Liu, A. Xiao and L. Su, Journal of Applied Mathematics, 2013 (2013) 9.

19. H. N. Caglar, S. H. Caglar, and E.N. Twizell. Applied Mathematics Letters, 12(5) (1999) 25.

PK ISSN 0022- 2941; CODEN JNSMAC
Vol. 57, (2017) PP 19-28

STUDY OF EFFECT OF VARYING FOCUS SHOTS ON STRUCTURAL AND MORPHOLOGICAL CHANGES InN FILMS

HAFIZ MUHAMMAD ZEESHAN

ABSTRACT

Effect of focus shots on deposited indium nitride films is studied on Si substrate using plasma focus device. Indium nitride is found to be maximum for 2 focus shots and silicon recrystallized and plane reflection (400) transforms to (220) plane. Morphological studies showed nano-ribbons for sample treated with higher focus shots of 6 and 8 focus shots. Electron dispersive X-ray spectroscopy (EDX) analysis showed maximum At% of indium content for 2 focus shots. Band gap is found to vary from 2.13 to 2.18 eV for various focus shots using ellipsometry.

INTRODUCTION

Indium Nitride is one of the important materials because it has wide range of applications due to its narrow and direct band gap, good mechanical properties, high thermal conductivity and high electrical resistivity [1-2]. Indium nitride has numerous applications such as ultra violet blue light emitting diodes, laser diodes, solar cells and optical wave guides. Since InN has low dissociation temperature, therefore high crystallinity is difficult to achieve [3-4]. Furthermore, indium nitride has diverse advantages in high frequency devices due to good transport characteristics over GaN and GaAs [5]. Indium nitride has been deposited by Plasma Assisted Molecular Beam Epitaxy (PAMBE) [6-11], Plasma assisted CVD [12-13], vapor phase epitaxial technique [14], reactive evaporation [3], Thermal Chemical Vapor Deposition [15], radio frequency metalorganic molecular beam epitaxy [16], RF sputtering [17], and pulsed laser deposition (PLD) [18]. Plasma focus device is used as deposition source. It is the source of pulsed X-rays [19], relativistic electrons, energetic ion beam [20-21] and neutrons [22-23]. Various workers had used it for thin film deposition and surface modification [24-27].

EXPERIMENTAL SETUP

The Dense plasma focus device is used for the deposition of InN on Si substrate. Samples are obtained by cutting them from Si wafer which are cleaned with acetone and then in ultrasonic bath for fifteen minutes. Mather type DPF device of energy is used for deposition process. Device parameters are given in previous papers [28]. The Schematic of system is shown in Figure 1.

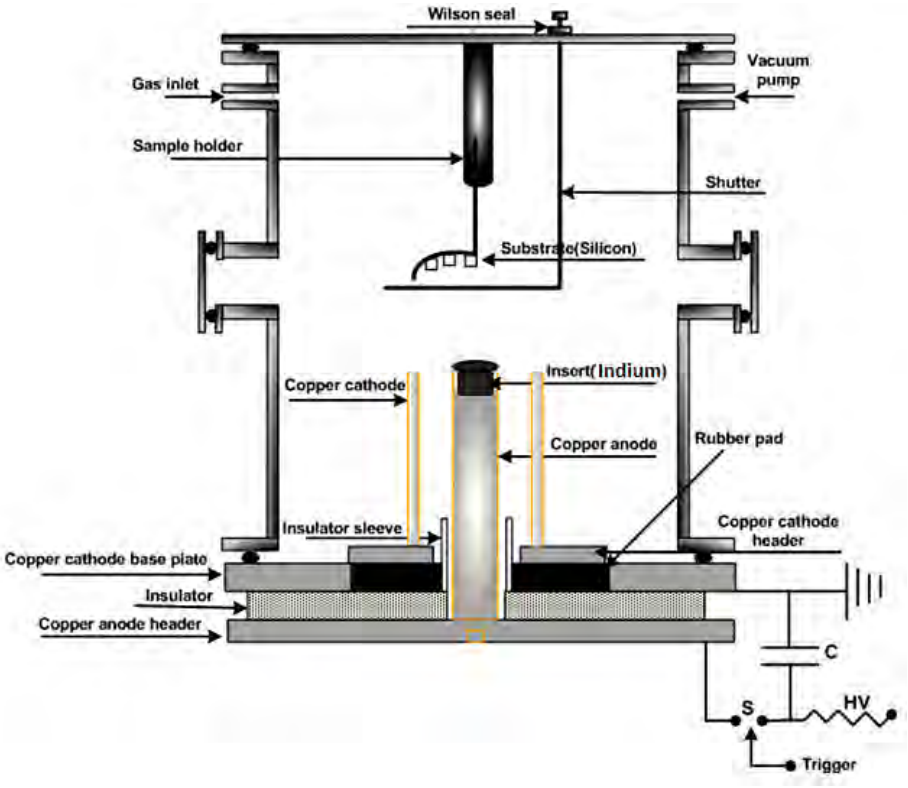

Figure 1: Schematic diagram of dense plasma focus system

Mather type Plasma focus device has coaxial symmetry in which anode is centered while having six electrodes around it which have equal space among themselves. Indium target was placed at the top of the hollow anode of copper. Nitrogen ambient environment is used for the desired film deposition. Low pressure upto 1 x 10^{-2} mbar is achieved into chamber by means of rotary pump. The pressure of ambient gas is kept constant at 1.25 m bar. The distance between target and substrate is kept 9 cm throughout the experiment. Si substrate is placed at substrate holder above the anode which is covered by shutter. Purpose of the shutter was to avoid exposure of substrate during the trial focusing as shown in Figure 1. Rogowski coil and high voltage probe are used to monitor the focusing of device. Frequency of focus shots is kept one focus shot per minute. It is enough for the thermal relaxation of substrate which is heated by the interaction of energetic ion beam with the substrate.

The working of the device is as follows: high energy stored capacitor is discharged across the device through spark gap. This sudden high voltage discharge initiates the breakdown of gas which occurs along the insulator surface. This forms the current sheath between anode and cathode having azimuthal symmetry. Current sheath moves axially towards the upper end of anode under JxB force where it pinches radially inward forming a focus shot which has highly energetic and dense beam of ions and electrons [29]. These relativistic electrons ablate the target (indium) materials which interact with nitrogen plasma forming InN. InN is directed towards the

substrate with the help of ions. Highly energetic ions move towards the substrate where they can either implant or re-sputter the deposited material.

Indium target is used as an insert in the anode. Films are deposited for 2,4,6 and 8 focus shots. XRD, SEM, EDX and ellipsometry are used to characterize the structural, morphological, elemental and bandgap of the deposited film respectively.

RESULTS AND DISCUSSIONS

Figs. 2 and 3 show the XRD spectra of untreated and treated samples Si (400) with only one peak at angle of 69.7degree. Diffraction peak of hexagonal InN is observed having preferred orientation along the phase of (101) plane which appears for of all samples treated at different focus shots [12]. Ion assisted recrystallization [30] results in the transformation of Si from (400) to (220) [31]. This structural analysis is also in agreement with the Inorganic Crystal Structure Database (ICSD).

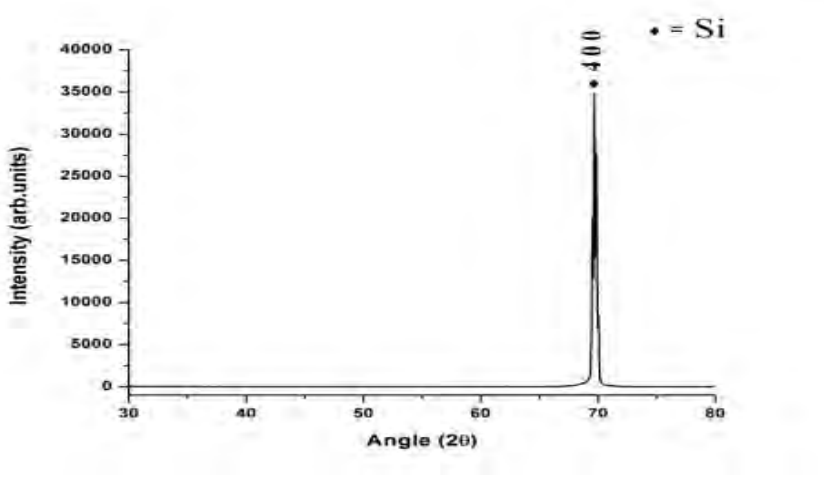

Figure 2: XRD spectra for Silicon

The good crytallinity for InN is observed for two focus shots only but it decreases with the shots. CuO is also found with phases of (-111) and (111) planes for two focus shots which may be due to the interaction of sputtered copper from anode and residual gases present in the chamber.

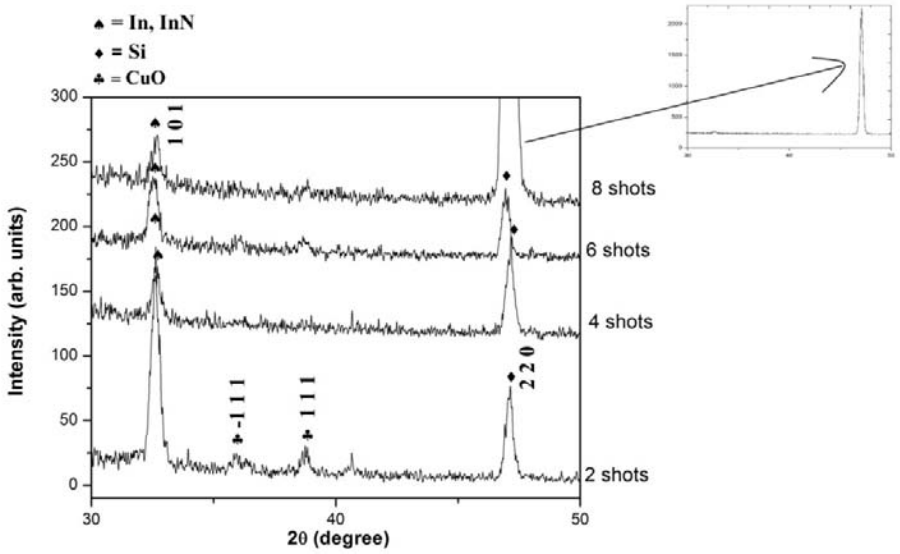

Figure 3: XRD spectra for various shots

Peak shift is observed towards lower angles which are due to the thermal shocks [14]. When high energetic ions strike the substrate, they penetrate into the substrate by ion implantation and diffusion causing defects which in turn develop stresses in the film resulting in peak shift.

Figure 4 shows relation between diffraction peak intensity and number of shots. A sudden decrease in intensity is observed from 2 to 4 focus shots which are due to re-sputtering.

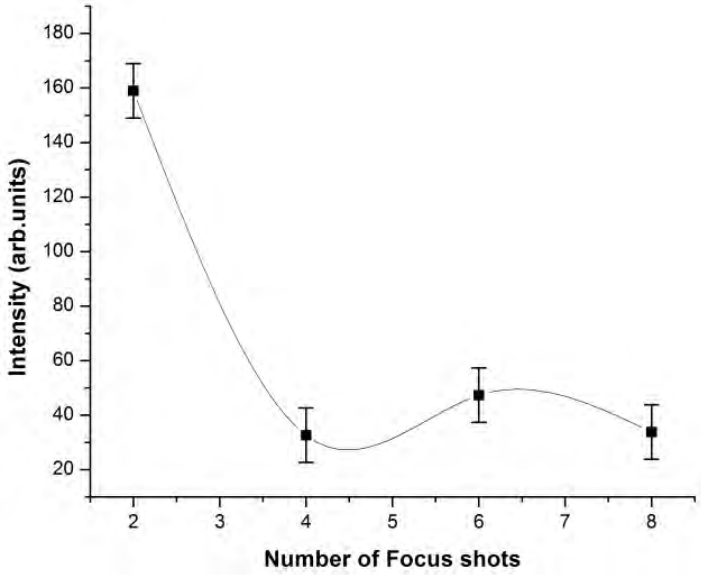

Figure 4: Plot between Number of focus shots and diffraction peak intensity

It is the observed that the film growth is dominant up to 2 focus shots while re-sputtering phenomenon and amorphization becomes dominant with increase in nitrogen dose. This lowers the crystallinity of the film due to nitrogen enrichment which may also be related with the rise of temperature.

The residual stresses have developed in the film which can be calculated using the relation given below:

$$\textbf{Stress} = \frac{\Delta d}{d} \textbf{ x E}$$

Where, **E** = Young's modulus = 149 GPa [32] and

$$\frac{\Delta d}{d} = \frac{d(observed) - d(ICSD)}{d(ICSD)} \textbf{= Strain}$$

d = Interatomic Distance and $d(ICSD)$ = Strain free interatomic spacing

The calculated stresses are plotted in figure 4. All stresses are tensile. Although tensile stresses remain almost constant from 2 to 6 focus shots but a drastic improvement in stresses is found for 8 focus shots which reveals the phenomenon of stress relaxation as observed in inset of figure 3.

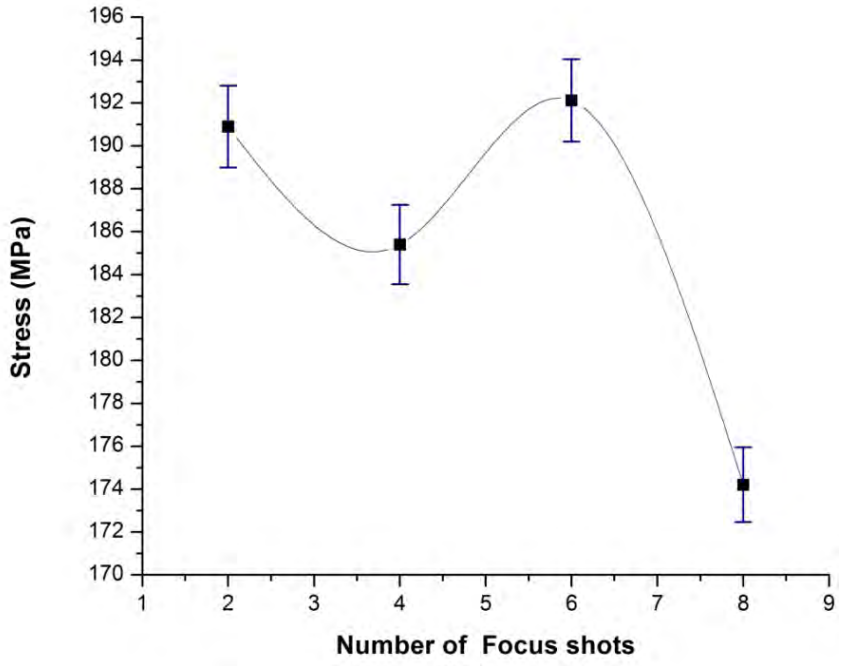

Figure 5: Effect of Stress by increasing Number of Focus shots

The reason of this behavior is plasma assisted annealing due to which Si recrystallization is found maximum for 8 focus shots.

SEM ANALYSIS

Figure 6 shows the surface morphology of Silicon substrate used in the experiment.

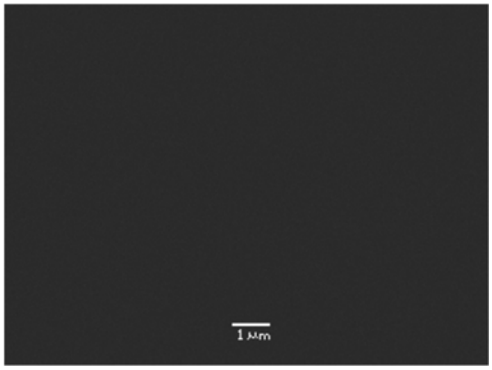

Figure 6: SEM image of untreated Silicon

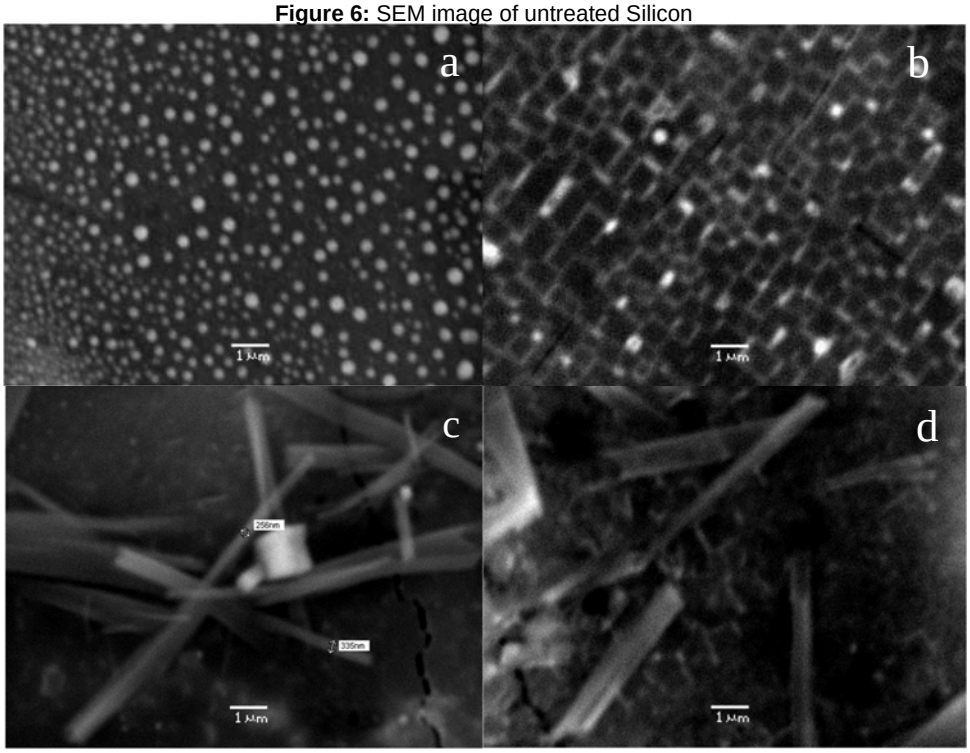

Figure 7: a, b, c and d show SEM micrograph of samples treated with 2, 4, 6 and 8 focus shots respectively

Scattered nano-grains are found in the SEM micrograph of sample treated with 2 focus shots as shown in fig 7 (a). The grains are distributed uniformly having sizes of 50 nanometers to 500 nanometers. With the increase in nitrogen and material flux, these grains grow to agglomerate forming continuous film for 4 focus shots. Nitrogen rich environment assists the formation of smaller rod like structure having void spaces which can be seen in SEM image of 6 and 8 focus shots. Chang et al [12] controlled the temperature and observed the transformation of InN nanowires into nano-ribbons. Here, only ribbons are found, as we know that temperature is high which is suitable for nano-ribbons formation. Cracks are also observed in 4, 6 and 8 focus shots images which are result of tensile stresses.

Electron Dispersive X –ray (EDX) Analysis

Table 1 shows the EDX data of sample treated with various focus shots. This data is collected from the backscattered detector of SEM.

Table 1: EDX analysis of InN/Si treated with various focus shots

Elements	2 Focus Shots	4 Focus Shots	6 Focus Shots	8 Focus Shots
	At %	At %	At %	At %
In	0.95	0.08	0.30	Negligible
Si	89.64	99.12	96.71	24.16
N	9.41	---	---	43.21
O	Negligible	0.80	2.99	32.62

Indium percentage has been found maximum for 2 focus shots and it is decreased further by increasing shots and diminishes at 8 focus shots. This behavior is due to the low decomposition temperature of indium nitride. On the contrary, Nitrogen concentration is found maximum for 8 focus shots which reveals that the ion implantation is dominant at higher shots which is suitable for recrystallization of Si. So, lower focus shots seem better for film deposition while ion implantation is better for higher focus shots. Moreover, oxygen content shows a tremendous increase at 8 focus shots. This shows that the repetition of focus shots results in the heating of the chamber which in turn results in the activation of burial gases. Although higher focus shots are found to be good for ion implantation but they also brought high concentration of impurity.

BAND GAP MEASUREMENT USING ELLIPSOMETRY

Ellipsometry is used to determine the band gap that is plotted in figs. 9.

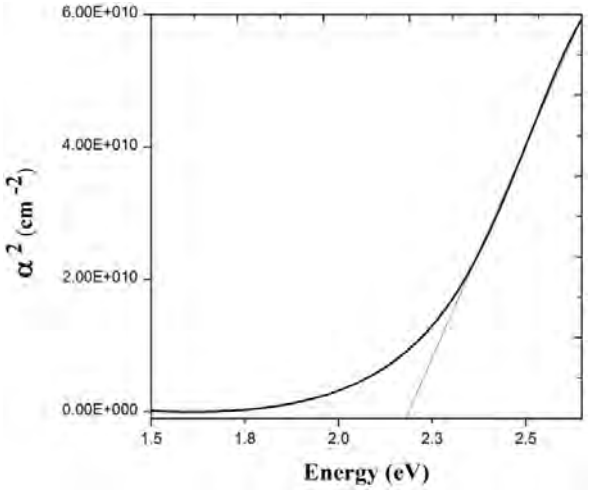

Figure 9: Bandgap for sample treated with 2 focus shots

Figure 9 shows the Tauc plot between α^2 and Energy. The x-intercept of this plot tells the band gap of the material. From the plot calculated band gap is 2.18 eV which is approximately same as reported in [17]. The plot between α^2 and Energy is nearly

linear. It is the evidence of the direct band to band transition. The band gap remains almost constant (2.13-2.18 eV) for various focus shots. This value is much higher than the predicted earlier [33, 34] for pure indium nitride. Higher value is due to the presence of oxygen and oxynitride in the indium nitride. Another reason which is found is the Burstein–Moss effect in which band gap is shifted towards the higher energies due to the dopants [33, 34].

CONCLUSION

InN films have been deposited on silicon substrate using plasma focus device for various focus shots. XRD analysis has confirmed the deposition of InN (101) having tensile stresses. 2 focus shots treatment is found to be good for deposition to achieve good crystalline quality. SEM analysis shows the nano-ribbons formation depending upon the nitrogen flux. EDX analysis has revealed that deposited films have maximum at % of indium for 2 focus shots. Bandgap is found in the range 2.13-2.18 eV.

REFERENCE

[1] S. Yamaguchi, M. Kariya, S. Nitt, T. Takeuchi, C. Wetzel and H. Amano, J Appl. Phys., 85 (1999) 7682.

[2] A. G. Bhuiyan, A. Hashimoto and A. Yamamoto, J. Appl. Phys., 94 (2003) 2779.

[3] Y. Saito, H. Harima, E. Kurimoto, T. Yamaguchi, N. Teraguchi and A. Suzuki, Phys. Stat. Sol. (b)., 234 (2002) 796.

[4] Y. Saito, Y. Tanabe, T. Yamaguchi, N. Teraguchi, A. Suzuki and T. Araki, Phys. Stat. Sol. (b), 240 (2003) 429.

[5] Sheetal J.Patil, Dhananjay S. Bodas, A. B. Mandale and S. A. Gangal, Journal of Thin solid Films, 444 (2003) 52.

[6] Chien-Huang Tsai, Vacuum 86 (2012) 1328.

[7] Mahesh Kumar, Thirumaleshwara N. Bhat, Mohana K. Rajpalke, Basanta Roul, A.T. Kalghatgi and S.B. Krupanidhi, Journal of Alloys and Compounds 513 (2012) 6.

[8] Junichi Sakaguchi, Tsutomu Araki, Tatsuya Fujishima, Elison Matioli, Tomas Palacios and Yasushi Nanishi, Japanese Journal of Applied Physics, **52** (2013) 08JD061.

[9] Mahesh Kumar, Basanta Roul, Thirumaleshwara N. Bhat, Mohana K. Rajpalke, Neeraj Sinha, A. T. Kalghatgi and S. B. Krupanidhi, J. Nanopart Res., **13** (2011) 1281.

[10] Neeraj Sinha, V. M. Jali, Thirumaleshwara N. Bhat, Basanta Roul, Mahesh Kumar, Mohana K. Rajpalke and S. B. Krupanidhi, AIP Conf. Proc., **1393** (2011) 77.

[11] Robert J. Kinsey, Phillip A. Anderson, Chito E. Kendrick, Roger J. Reeves and Steven M. Durbin, Journal of Crystal Growth, **269** (2004) 167.

[12] Yi-Kuei Chang and Franklin Chau-Nan Hong, Materials Letters, **63** (2009) 1855.

[13] P. P. T. Chen, J. E. Downes, A. J. Fernandes, K. S. A. Butcher, M. Wintrebert-Fouquet, R. Wuhrer and M. R. Phillips, Thin Solid Films **519** (2011) 1831.

[14] W. Z. Shen, Z. W. Jia, J. Chen, H. B. Ye, H. Ogawa and Q. X. Guo, Journal of Crystal Growth, **298** (2007) 394.

[15] Ming-Shien Hu, Wei-Ming Wang, Tzung T. Chen, Lu-Sheng Hong, Chun-Wei Chen, Chia Chun Chen, Yang-Fang Chen, Kuei-Hsien Chen and Li-Chyong Chen, Adv. Funct. Mater., **16** (2006) 537.

[16] Wei-Chun Chen, Shou-Yi Kuo, Wei-Lin Wang, Jr-Sheng Tian, Woei-Tyng Lin, Fang-I Lai and Li Chang, Nanoscale Research Letters, **7** (2012) 468.

[17] K. S. A. Butcher, M. Wintrebert Fouquet, P. P.T. Chen, T. L. Tansley, H. Dou, S. K. Shrestha, H. Timmers, M. Kuball, K. E. Prince and J. E. Bradby, J. Appl. Phys. **95** (2004) 6124.

[18] F. Stokker-Cheregi, A. Nedelcea, F. M. Voicu, D. M. Marin, R. Bîrjega and M. Dinescu, Romanian Reports in Phy., **65** (2013) 213.

[19] S. Hussain, S. Ahmad, M. Sharif, M. Sadiq, A. Waheed and M. Zakaullah, Phys. Lett. A, **349** (2006) 236.

[20] H. R. Yousefi, S. R. Mohanty, Y. Nakada, H. Ito and K. Masugata, Phys. Plasmas **13** (2006) 114506.

[21] L. Soto, Plasma Phys. Controlled Fusion, **47** (2005) A361.

[22] M. Zakaullah, A. Waheed, S. Ahmad, S. Zeb and S. Hussain, Plasma Sources Sci. Technol., **12** (2003) 443.

[23] J. M. Koh, R. S. Rawat, A. Patran, T. Zhang, D. Wong, S.V. Springham, T. L. Tan, S. Lee and P. Lee, Plasma Sources Sci. Technol., **14** (2005) 12.

[24] Tousif Hussain, R. Ahmad, I. A. Khan, Jamil Siddiqui, Nida Khalid, Arshad Saleem Bhatti, Shahzad Naseem, Nuclear Instruments and Methods in Physics Research B, **267** (2009) 768.

[25] M. T. Hosseinnejad, M. Ghoranneviss, G. R. Etaati, M. Shirazi and Z. Ghorannevis, Applied Surface Science, **257** (2011) 7653.

[26] M. Valipour, M. A. Mohammadi, S. Sobhanian and R. S. Rawat, J. Fusion Energy, **31** (2012) 65.

[27] M. Hassan, A. Qayyum, R. Ahmad, G. Murtaza, M. Zakaullah, J. Phys. D: Appl. Phys., **40** (2007) 769

[28] S. Lee, T.Y. Tou, S.P. Moo, M.A. Eissa, A.V. Gholap, K.H. Kwek, S. Mulyodrono, A.J.Smith, Suryadi, W. Usada and M. Zakaullah, Am. J. Phys., **56** (1988) 62

[29] Tousif Hussain, R. Ahmad, I.A. Khan, Jamil Siddiqui, Nida Khalid, Arshad Saleem Bhatti and Shahzad Naseem, Nuclear Instruments and Methods in Physics Research B, **267** (2009) 768

[30] M. Hassan, A. Qayyum, R. Ahmad, R.S. Rawat, P. Lee, S.M. Hassan, G. Murtaza and M. Zakaullah, Nuclear Instruments and Methods in Physics Research B, **267** (2009) 1911.

[31] E. A. Odo, D. T. Britton, G. G. Gonfa and M. Harting, The African Review of Phy., **7** (2012) 7.

[32] V. N. Gurarie, P. H. Otsuka, D.N. Jamieson and S. Prawer, Nucl. Instr. Meth. Phys. Res. B, **242** (2006) 421.

[33] V. Yu. Davydov, A. A. Klochikhin, R. P. Seisyan, V. V. Emtsev, S. V. Ivanov, F. Bechstedt, J. Furthmuller, H. Harima, A. V. Mudryi, J. Aderhold, O. Semchinova and J. Graul, Phys. Stat. Sol. (b), **229** (2002) R_1- R_3.

[34] B. Monemar, P. P. Paskov and A. Kasic, Superlattices and Microstructures, **38** (2005) 38.

PK ISSN 0022- 2941; CODEN JNSMAC
Vol. 57, (2017) PP 29-37

PLASMA ASSISTED DEPOSITION OF INDIUM OXIDE THIN FILMS ON STAINLESS STEEL USING DENSE PLASMA FOCUS DEVICE

FALAK SHER[a]; TOUSIF HUSSAIN[b]; JAMIL SIDDIQUI[b] and RIAZ AHMAD[c]

[a]Govt. Degree College, Narang Mandi, district Sheikhupura

[b]Centre for Advanced Studies in Physics (CASP), GC University Lahore

[c]Department of Physics, GC University Lahore

ABSTRACT

Plasma assisted growth of Indium Oxide thin films on Stainless Steel (SS-306) substrate using Mather type dense plasma focus device is reported here. Effect of variation in number of plasma focus shots on structural, morphological and compositional characteristics of synthesized thin films have been investigated. The film structure and chemical composition were characterized by using X-ray diffraction (XRD) and Fourier Transform Infrared Spectroscopy (FTIR). The surface morphology was investigated by Scanning electron microscopy (SEM). The XRD results suggested the formation of Indium oxide thin film on SS-306 substrate with crystal planes (222), (110), (420), (332) and (642). Indium and oxygen bonding is confirmed by FTIR is appearing at wave number 700 to 900 cm^{-1}. SEM analysis showes combination of uniform and rough surface of the deposited thin films with indium oxide particles on substrate surface diffused together at various number of focus shots.

Keywords: Indium Oxide thin films; DPF; XRD; SEM

INTRODUCTION

Indium oxide is transparent conducting oxide (TCO) material that has wide range of applications in photo electronic devices, flat panel display, thin film transistor, electroluminescent devices, photovoltaic cells, gas sensors sand light emitting diodes [1–3]. In_2O_3 has a direct band gap of about 3.7 eV [4] and an indirect band gap of about 2.6 eV [5]. Indium oxide thin films have unique properties such as high optical transparency and high electrical conductivity are extensively used in many applications.

A variety of techniques employed to fabricate In_2O_3 thin films such as reactive thermal evaporation [6], ion beam sputtering [7], pulsed laser deposition (PLD) [8], chemical vapor deposition [9] and thermal evaporation [10–12] reveal that the principal factors affecting the structural, optical and electrical properties of such films include the method of preparation, substrate temperature, rate of deposition,

composition, film thickness, partial pressure of oxygen and post deposition annealing processes.

The dense plasma focus (DPF) device is a hydro magnetic coaxial plasma accelerator where the high-current electrical discharge efficiently heats and compresses the plasma into a pinched plasma column where a short lived hot (1 keV–2 keV) and dense (10^{25} m^{-3}–10^{26} m^{-3}) plasma is produced. The energy density of the DPF device is reported to be in a range of 1.2×10^{10} J/m^3–9.5×10^{10} J/m^3, which makes it a high energy plasma facility. [13] The dense and hot plasma produced by the device has also been acknowledged as a multi radiation source of highly energetic ions, [14] relativistic electrons, [15,16] neutrons, [17] and intense bursts of x-rays.[18] Due to the broad energy spectrum of radiation emanated in the plasma focus, its application in material processing has shown prominent features of better adhesion and good deposition rates [19, 20]. Numerous properties and features of DPF, which have made it an exclusive and attractive source for thin film depositions and material processing, have been reported by Rawat in a recent review paper.

EXPERIMENTAL SETUP

The system of Plasma Focus is energized through capacitor of capacitance 32 μF, 15 kV maximum 3.6 kJ and it is charged at the voltage of 12 kV (2.3 kJ). This is giving maximum discharge current approximately about 175 kA. The capacitor charges to the voltage to 12 kv by using charging unit and it is discharged across the load by using high power switch.

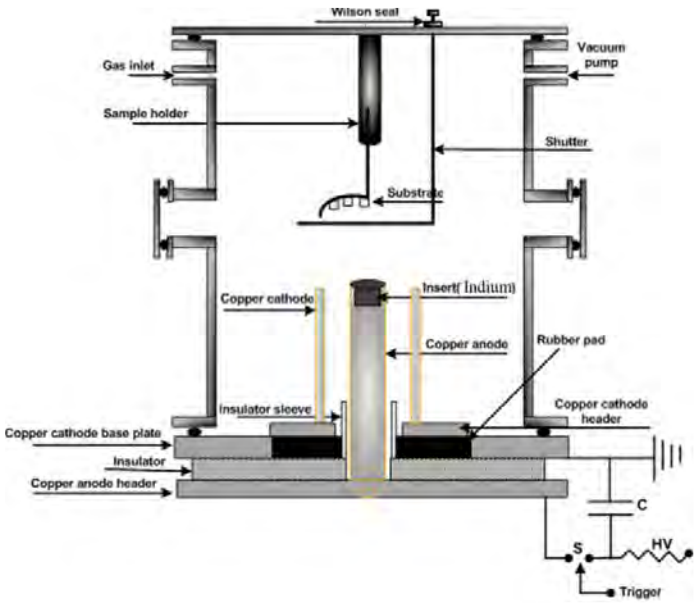

Figure 1: The Schematic Diagram of Dense Plasma Focus

In Initial Break down phase capacitor bank is discharged through a spark gap which creates high pulsating potential difference between coaxial electrodes in the chamber filled with gas at the optimum pressure. The breakdown of gas takes place

instantaneously. This breakdown results in the formation of an axis symmetric current sheath, which is influenced and accelerated by the Lorentz force. The current sheath spreads uniformly outwards towards the cathode rods in an inverse pinch phase and then accelerates upwards towards the open end of the electrodes in an axial run down phase. The sheath collapses radially inwards on reaching the open end of electrode assembly, resulting in the creation of short lived (~1–50 ns), dense (~10^{26} m^{-3}) and hot (~1 keV) pinched plasma just above the anode tip in the final focus phase.

In Pinched plasma column the induced electric field is enhanced locally, that couples with the magnetic field, resulting in the disruption of the plasma column due to sausage (m=0) instability [21]. The disruption of the plasma column leads to the acceleration of highly energetic ions towards the top of the chamber, and relativistic energies electrons (100 keV above) in the downward direction towards the positively charged anode.

Indium oxide thin films were deposited on Stainless Steel (SS-306) substrate using DPF (dense plasma focus) device. Indium as a target and SS-306 as a substrate material are utilized. Oxygen gas was used as a reactive gas for the formation of indium oxide thin films. Plasma was generated in Mather type plasma focus device. The samples were treated for different number of focus shots (2, 5, 8 and 11) at 0^{o} on the axis and 10 cm away from anode's tip. The treated samples were analyzed using X-Ray diffraction (XRD), FTIR spectroscopy and scanning electron microscope (SEM).

RESULTS AND DISCUSSIONS

Structural analysis of Indium Oxide Thin Films (XRD)

Structural analysis was performed using X Pert PRO (MPD) X-Ray diffractromter. The difractrometer was operated at 40 kV and 40 mA using kα source (1.5406 Å).

Figures 2 and 3 show the XRD patterns of unexposed and exposed samples. The XRD pattern for the unexposed sample confirms the signatures of FCC (face centered cubic) austenitic stainless steel (γ-Fe) phase and a BCC (body centered cubic) ferritic iron (α-Fe) phase. The plane reflections (111), (200) and (220) are related to the γ-Fe phase while (110) and (200) plane reflections are corresponding to α-Fe phase. The increase in temperature during manual polishing may cause stress induced transformation of gamma to alpha phase [73, 74].

Figure-3 shows the XRD patterns of the samples treated at 0° angular position for various numbers of focus shots (2, 5, 8 and 11). The emergence of indium oxide crystalline phases for all the exposure conditions confirms the deposition of indium oxide on stainless steel substrate. For two focus shots, seven new diffraction peaks corresponding to plane reflections of (222), (110), (104), (110), (103), (600), (640) of In_2O_3, Cr_2O_3 and Cr_2O_5 phases are appeared respectively. For 5 number of deposition focus shots the intensity of diffraction peaks of In_2O_3 and Cr_2O_3 phases

increases indicating the improvement in crystallanity [73] with increase in number of focus shots. Moreover peak corresponding to (222) and (103) reflection planes disappears with the emergence of In_2O_3 phase corresponding to (332) reflection plane, which suggests the growth of one phase at the expense of the other [74]. It is interesting that the intensity of (110) In_2O_3 reflection plane is stronger than any of the other emerged phases. This shows that the quantity of In_2O_3 phase is more as compared to that of other phases at the top surface of the exposed samples except Stainless Steel peak. For 8 and 11 number of focus shots the peak corresponding to (222) plane reflection reappears along with reduction in intensities of most of the peaks.

Upon exposure the intensities of interface peaks related to γ-Fe and α-Fe reflection planes are decreased. Moreover there are considerable shifts in the γ-Fe phases which may be due to the residual stresses induced in the deposited films. From the above discussion we can say that that the indium oxide film formation in the present work is not only because of the implantation of the energetic oxide ions on the SS-306 substrate but also due to the deposition of sputtered indium. If the route is only the ion implantation then one would expect the formation of only In_2O_3. This confirms that plasma focus assisted thin film deposition is the combination of two different processes: the ion implantation and re-deposition of ion beam ablated backscattered species. The rise in substrate temperature may result in the formation of Indium Oxide peaks as oxygen is reactive. So it can react with substrate at favorable conditions (rise in substrate temperature) which results in the formation of interface peaks (Cr_2O_3 and Cr_2O_5).

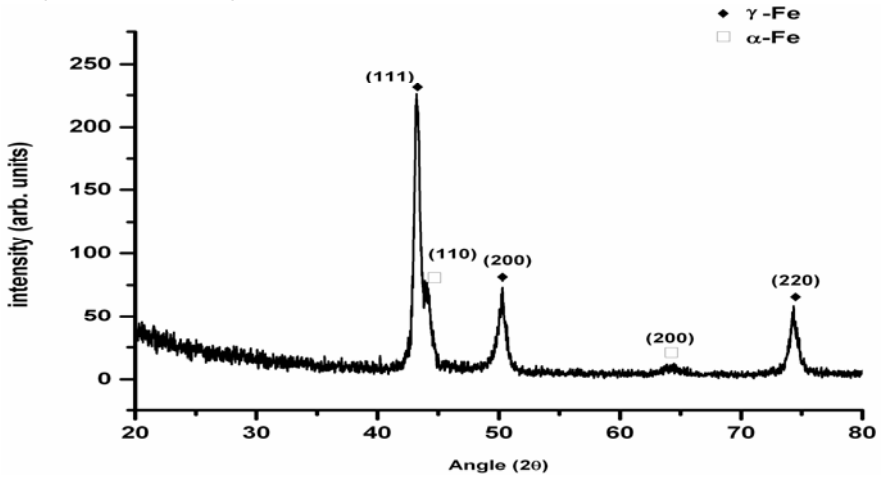

Figure 2: XRD pattern of untreated SS-306

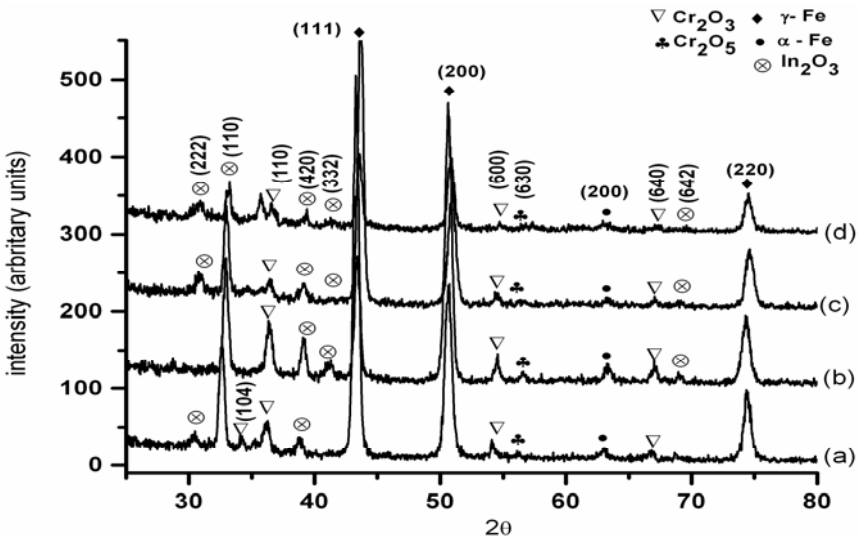

Figure-3: XRD pattern of exposed SS-306 for various number of focus shots (a) 2 shots (b) 5 shots (c) 8 shots (d) 11 shots

FTIR SPECTROSCOPY

For Chemical analysis of Indium oxide thin films on SS-306 substrate was performed by IRPrestige-21 Shimadzu FTIR Spectrometer in the ATR mode for spectral range from 650-4000 cm^{-1}. The ATR-FTIR was performed with 25 scans repetition and with 4 cm^{-1} resolution. The recorded FTIR Spectra for untreated and exposed SS-306 substrate shown in Figure 4.

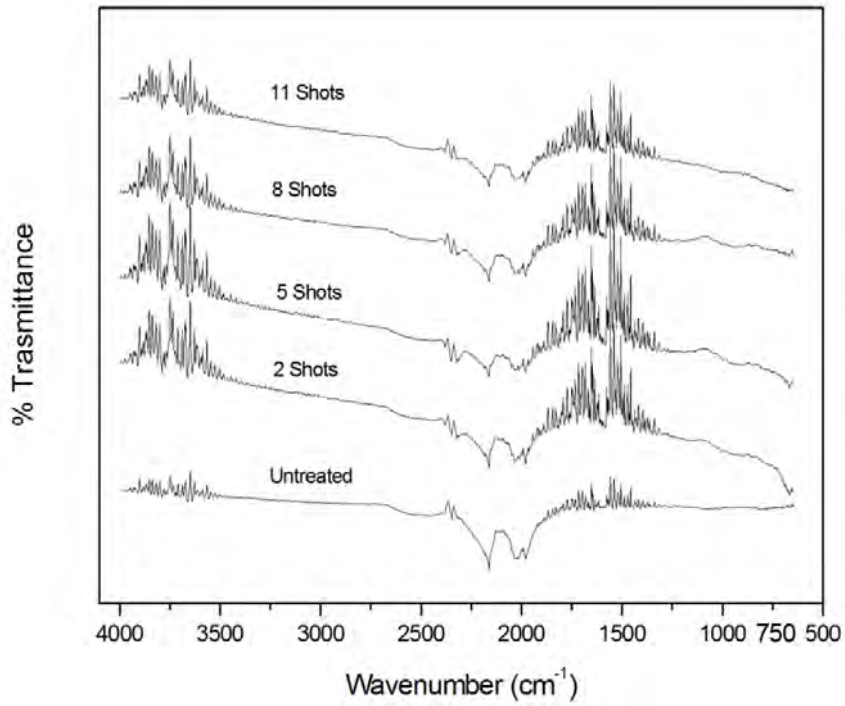

Figure 4: FTIR spectra of untreated SS-306 and Indium oxide thin films deposited on SS-306

The band positions and number of transmittance peaks are dependent on crystal structure, chemical composition and on the morphology of the deposited thin films

[22]. Untreated SS-306 has range of transmittance peaks which correspond to its chemical composition. These peaks are due to the bonding of elements present in SS-306 with Carbon and oxygen and inter elemental bonding. A band is also observed in the wavenumber range of 700 to 900 cm^{-1} which corresponds to the bonding of Indium and Oxygen bond and the peak at 732 cm^{-1} is attributed to the formation of In_2O_3 thin film [23].

The given spectra have one small peak of CO_2 at 2357 cm^{-1}. CO_2 flows through the sample cell due to the cavity formed between the sample surface and ATR Crystal and absorbs IR light [24].

Table 1: IR frequencies and band assignments for the In_2O_3 thin films deposited on SS-306 for varying focus shots.

Wavenumber (cm^{-1})	Band Assignment
700-900	In-O
732	In_2O_3
1200-2300, 3500-3800	Related to elements present in SS-306
1430	C = C
2360	CO_2

The peak at 732 cm^{-1} is attributed to the formation of In_2O_3. Small peak at 2360 cm^{-1} arises due to contamination during analysis. By increasing the focus shots, similar kind of spectra is formed.

MORPHOLOGICAL ANALYSIS

The surface morphology of the indium oxide thin films deposited on SS-306 substrate with different number of focus shots (2, 5, 8 and 11) at the axis is exhibited in Figure 5.

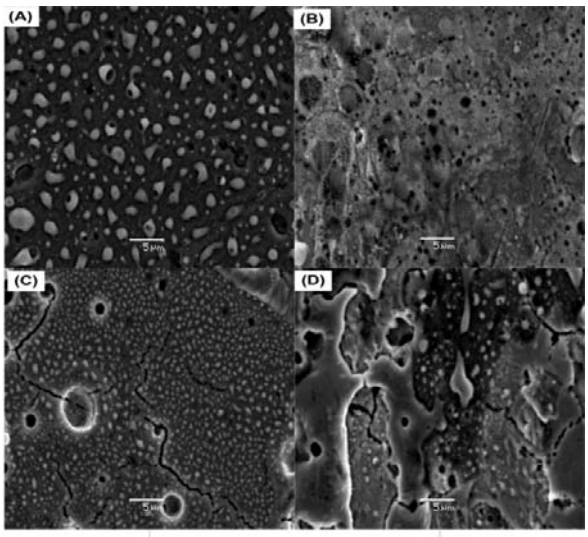

Figure 5: SEM micrograghs for various number of focus shots (A) 2 Shots (B) 5 Shots (C) 8 Shots and (D) 11 Shots

The absence of scratches in the treated samples morphology provides the evidence for the formation of indium oxide films fully covered the samples surfaces. For 2 focus shots (Fig. 5 A) a large number of indium oxide /chromium oxide nano particles are distributed unevenly on the subsurface of the deposited films. These particles do not cover the whole surface of the film, showing that microstructure of the top surface is less dense in nature. For 5 focus shots Fig. 5 B, the micrograph shows relatively smooth surface morphology but few voids are present in the film. The sudden change in surface morphology and emergence of irregular pores/voids may be due to energetic ions irradiation followed by successive focus shots. The rise in surface temperature may be another reason for melting the surface. The surface morphology of the film deposited with 8 focus shots changes significantly as it becomes rougher and consists of cracks and relatively small sized particle, distributed evenly on the entire surface. These structures may be developed due to transfer of sufficient ion energy to the sample surface. For each focus shot the sample is exposed with pulsed energetic ion beam (with approximately 100 ns pulse duration and the energy range of ions is 38 keV to 1.6 MeV) which may cause transient sample surface heating approximately up to several thousand degrees centigrade in a short time and is followed by fast melting and re-solidification [26]. Sudden re-solidification leads to the crack formation on the surface of deposited films. We can say that the process of ion irradiation is equivalent to the transient thermal annealing and results in rearrangement of atoms in the layers of the surfaces. This transient thermal annealing by means of pulsed ion beam causes atomic diffusion on surface layer after focusing. That is why 8 focus shots irradiation significantly changes the surface morphology. Again for 11 focus shots cracks can be observed in the deposited film with irregular swollen surface.

By the bombardment of energetic oxygen ions sufficient amount of energy may transfer to the sample surface that initiates the nucleation of new compounds. With increasing number of focus shots the film develops through nucleation in different forms depending on successive focus shots. It is reported that growth of rough surfaces is quicker in comparison with growth smooth surfaces. At low substrate temperature, surfaces are almost smooth (Fig. A, B) but when the temperature is increased with number of focus shots, surfaces become rough [26] and swollen with cracks. These cracks are developed due to quenching and stresses present in the film.

CONCLUSIONS

Indium oxide thin films are deposited on Stainless steel (SS-306) substrate using Dense Plasma (DPF) device with various number of focus shots. XRD patterns of the exposed samples confirm the presence of Indium Oxide phases along with Chromium Oxide peaks for all conditions. The FTIR analysis also confirms the presence of

Indium Oxide. The SEM analysis shows that morphology of treated samples strongly depends on the number of plasma focus shots.

REFERENCES

1. Senthilkumar, V. and P. Vickraman, Current Applied Physics, **10**(3) (2010) 880-885.

2. C. Nunes de Carvalho, G. Lavareda, A. Amaral, O. Conde and A. R. Ramos, **352**(23) (2006) 2315-2318.

3. Lee, J. H., S. Y. Lee and B. O. Park, Materials Science and Engineering: B, **127**(2) (2006) 267-271.

4. P. Malar, B. C. Mohanty and S. Kasiviswanathan, Thin Solid Films, **488**(1) (2005) 26-33.

5. R. L. Weiher and R. P. Ley, Journal of Applied Physics, **37**(1) (1966) 299-302.

6. C. A. Pan and T. P. Ma, Applied Physics Letters, **37**(2) (1980) 163-165.

7. J. S. Cho, K. H. Yoon and S. K. Koh, Journal of Applied Physics, **89**(6) (2001) 3223-3228.

8. E. J. Tarsa, M. De Graef, D. R. Clarke, A. C. Gossard and J. S. Speck, Journal of Applied Physics, **73**(7) (1993) 3276-3283.

9. S. Suh and D. M. Hoffman, Journal of the American Chemical Society, **122**(39) (2000) 9396-9404.

10. Mihaela Girtan G. I. Rusu, G. G. Rusu and S. Gurlui, Applied Surface Science, **162-163** (2000) 492-498.

11. Z. Zang, A. Nakamura and J. Temmyo, Optics Express, **21**(9) (2013) 11448-11456.

12. Z. Zang, A. Nakamura and J. Temmyo, Materials Letters, **92** (2013) 188-191.

13. S. Leopoldo, Plasma Physics and Controlled Fusion, **47**(5A) (2005) A361.

14. H. Bhuyan, H. Chuaqui, M Favre, I. Mitchell and E. Wyndham, Journal of Physics D: Applied Physics, **38**(8) (2005) 1164.

15. H. R. Yousefi , S. R. Mohanty, Y. Nakada, H. Ito and K. Masugata, Physics of Plasmas, **13**(11) (2006) 114506.

16. M. Zakaullah, A. Waheed, Sarfraz Ahmad, Shaista Zeb and S. Hussain, Plasma Sources Science and Technology, **12**(3) (2003) 443.

17. J. M. Koh, R. S. Rawat, A. Patran, T. Zhang, D. Wong, S. V. Springham,T. L. Tan, S. Lee and P. Lee, Plasma Sources Science and Technology, 14 (2005) 12.

18. M. Shafiq, S. Hussain, A. Waheed and M. Zakaullah, Plasma Sources Science and Technology, **12**(2) (2003) 199.

19. R. S. Rawat, V. Aggarwal, M. Hassan, P. Lee, S. V. Springham, T. L. Tan and S. Lee, Applied Surface Science, **255**(5, Part 2) (2008) 2932-2941.

20. R. S. Rawat, M. P. Srivastava, S. Tandon and A. Mansingh, Physical Review B, **47**(9) (1993) 4858-4862.

21. W. Kies, G. Decker, U. Berntien, Yu V. Sidelnikov, D. A. Glushkov,K. N. Koshelev, D. M. Simanovskii and S. V. Bobashev, Plasma Sources Science and Technology, **9**(3) (2000) 279.

22. Prem Nath, R. F. Bunshah, B. M. Basol and O. M. Staffsud, Thin Solid Films, **72**(3) (1980) 463-468.

23. J. C. C. Fan and J. B. Goodenough, Journal of Applied Physics, **48**(8) (1977) 3524-3531.

24. G. Visco, L. Campanella and V. Nobili, Microchemical Journal, **79**(1) (2005) 185-191.

25. M. J. Marques, J. Pina, A. M. Dias, J. L. Lebrun and J. Feugeas, Surface and Coatings Technology, **195**(1) (2005) 8-16.

26. T. Mae, M. Nose, M. Zhou, T. Nagae and K. Shimamura, , Surface and Coatings Technology, **236 (**2001) 143-144.